ROYAL SOCIETY OF CHEMISTRY

PAPER

Check for updates

3D printing of superhydrophobic and multifunctional objects *via* simple and inexpensive vat photopolymerization†

Adil Majeed Rather, Mohammed Barrubeeah, Mohammad Javad Zarei, Young Jae Kim, Sravanthi Vallabhuneni and Arun Kumar Kota ⓘ *

3D printing has emerged as a revolutionary technology in the manufacturing industry, enabling the creation of complex and intricate structures with precision and accuracy. Among various 3D printing technologies, vat photopolymerization has several advantages including high precision, fast molding, and ambient temperature printing. In this work, we employed an inexpensive vat photopolymerization 3D printer (nearly an order of magnitude lower in cost compared to prior reports), with an ink that consists of only two commercially-available components (photopolymer resin and PVDF particles), and a process that consists of only two steps (photopolymerization and washing) to fabricate superhydrophobic 3D objects with complex shapes and geometries. Our intention here is to convey that fabrication of superhydrophobic objects *via* vat photopolymerization 3D printing is very forgiving and does not require expensive instrumentation or custom-made multi-component inks (>2 components) or multi-step processing (>2 steps). Furthermore, by modifying the inks with magnetic particles or photochromic/thermochromic dyes, we fabricated multifunctional 3D printed objects with superhydrophobicity as well as magnetic or color morphing properties. We envision that our simple and inexpensive 3D printing technique will democratize the fabrication of superhydrophobic and multi-functional objects by enabling access to a wide range of end-users, especially in cost-constrained or skill-constrained environments.

1. Introduction

3D printing has emerged as a revolutionary technology in the manufacturing industry due to its advantages like reduced waste, ease of customization, and design flexibility in fabrication of complex and intricate structures with precision and accuracy.[1–4] Among various 3D printing technologies, vat photopolymerization has several advantages including high precision, fast molding, and ambient temperature printing.[5–10] As a result, recently, a few researchers have used vat photopolymerization 3D printing to fabricate 3D structures or objects with superhydrophobicity (*i.e.*, extreme repellence to aqueous liquids).[11–14] Such superhydrophobic structures or objects are desirable for a wide range of applications including anti-biofouling, anti-corrosion, oil–water separation, microfluidic devices *etc.*[15–26] Unlike prior reports, in this work, we employed an inexpensive vat photopolymerization 3D printer (nearly an order of magnitude lower in cost compared to prior

reports), with an ink that consists of only two commercially-available components (photopolymer resin and PVDF particles), and a process that consists of only two steps (photopolymerization and washing) to fabricate superhydrophobic 3D objects with complex shapes and geometries. Our intention here is to convey that fabrication of superhydrophobic objects *via* vat photopolymerization 3D printing is very forgiving and does not require expensive instrumentation or custom-made multi-component inks (>2 components) or multi-step processing (>2 steps). Our superhydrophobic objects displayed super-repellency (*i.e.*, contact angle >150° and sliding angle <10°) for aqueous liquids of surface tension $\gamma_{lv} \geq 55$ mN m^{-1}, and allowed droplet manipulation on grooves with different geometries. Utilizing the selective repellency of our superhydrophobic objects to water ($\gamma_{lv} \approx 72$ mN m^{-1}), but not oils and organic solvents ($\gamma_{lv} < 30$ mN m^{-1}), we also demonstrated the selective absorption of oils and organic solvents from water. Furthermore, by modifying the inks with magnetic particles or photochromic/thermochromic dyes, we fabricated complex multifunctional 3D printed objects with superhydrophobicity as well as magnetic or color morphing properties. We envision that our simple and inexpensive 3D printing technique will democratize the fabrication of superhydrophobic and

Department of Mechanical and Aerospace Engineering, North Carolina State University, Raleigh 27695, USA. E-mail: akota2@ncsu.edu

† Electronic supplementary information (ESI) available. See DOI: https://doi.org/10.1039/d4nr05135a

multi-functional objects by enabling access to a wide range of end-users, especially in cost-constrained or skill-constrained environments.

To accomplish inexpensive and simple 3D printing of superhydrophobic objects, it is first essential to understand the underlying principles of wettability. The wettability of a liquid on a non-textured (or smooth) solid surface can be characterized by the equilibrium contact angle θ, given by the Young's equation.[27] A surface with $\theta > 90°$ is considered to be hydrophobic. Typically, materials with low solid surface energy γ_{sv} result in high θ.[28–30] However, even on the lowest γ_{sv} non-textured surfaces, the highest observed water contact angle $\theta \sim 130°$.[31] Higher contact angles can be achieved only with textured (or rough) surfaces.[32,33] When a liquid droplet contacts a textured surface, it displays the apparent contact angle $\theta*$ (different from equilibrium contact angle θ), and adopts one of two possible states – the Wenzel state[34] or the Cassie-Baxter state.[35] In the Wenzel state, the liquid penetrates the texture and wets the surface completely. In the Cassie-Baxter state, air pockets are trapped between the surface and the liquid; therefore, the liquid contacts both air and solid. The Cassie-Baxter state can lead to very high apparent contact angles $\theta*$ because the air pockets reduce the solid–liquid contact area and increase the solid-air contact area.[36,37] Furthermore, the Cassie-Baxter state results in low contact angle hysteresis (i.e., difference in advancing and receding contact angles), which in turn leads to low sliding angles ω (i.e., the minimum tilt angle when a droplet slides off from the surface).[38,39] As a result, the Cassie-Baxter state is preferred for designing superhydrophobic surfaces (i.e., surfaces with $\theta* > 150°$ and sliding angle $\omega < 10°$ for high surface tension liquid like water).[40–42] In order to achieve such a Cassie-Baxter state and superhydrophobicity, a combination of materials with low surface energy and appropriate surface texture is required.[41]

2. Results and discussion

Building on the above understanding, in this work, we used a very low-cost 3D printer to fabricate superhydrophobic objects. To put the inexpensive nature of the 3D printer into perspective, it is an order of magnitude lower in cost compared to all prior studies that used vat photopolymerization 3D printing to fabricate superhydrophobic structures or objects (materials and methods). For the ink, we modified the photopolymer resin by adding commercially available polyvinylidene difluoride (PVDF) particles (~10–20 μm in diameter) to impart low solid surface energy ($\gamma_{sv} \approx 25$ mN m^{-1}).[43] After 3D printing, we washed the objects with an appropriate solvent (e.g., acetone) to remove the unpolymerized photopolymer resin, resulting in a textured surface (Fig. 1). The combination of low surface energy imparted by PVDF and appropriate texture from washing resulted in superhydrophobicity.

The key parameters influencing the fabrication of superhydrophobic objects with the inexpensive 3D printer are composition of the ink (imparting low solid surface energy) and washing time (imparting texture). To systematically investigate the influence of ink composition on superhydrophobicity, we 3D printed simple cuboid-shaped objects with photopolymer resin + PVDF blends consisting of different PVDF compositions (0 wt% to 35 wt%), at a fixed washing time (60 min). To assess the wetting properties of the 3D printed cuboids, we measured the contact angles and sliding angles with ~20 μL water droplets (materials and methods). With just the photopolymer resin (i.e., 0 wt% PVDF), the surfaces of the 3D printed cuboids displayed low roughness (Fig. 2a; $R_{rms} = 16 \pm 1.8$ μm) and hydrophilicity with apparent contact angle $\theta* = 76°$ (Fig. 2d). Water droplets remained stuck to the surface even when the surfaces were vertical (i.e., no finite sliding angle). As the composition of PVDF increased, the surface
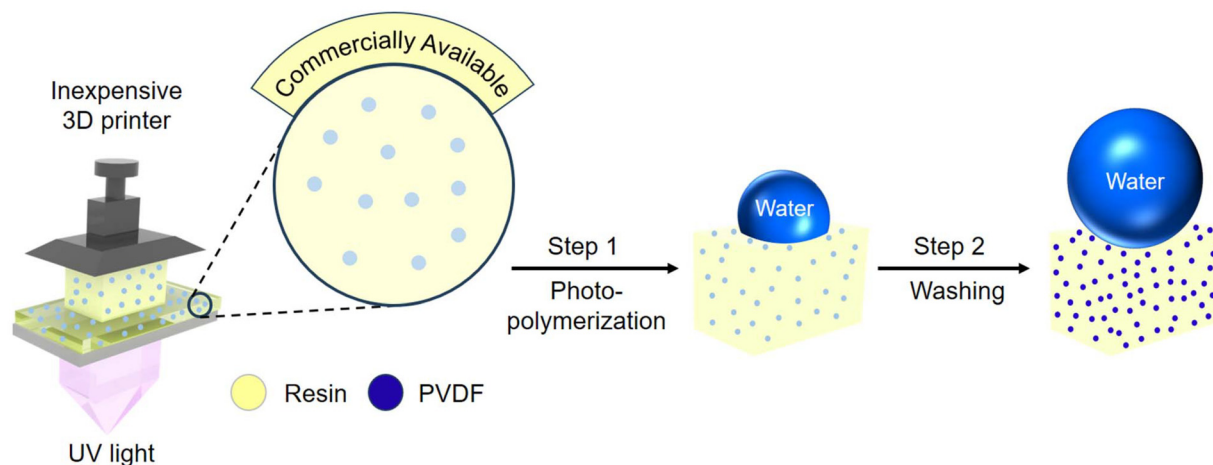

Fig. 1 Fabrication process. Schematic illustrating the fabrication of 3D printed superhydrophobic objects. PVDF represents polyvinylidene difluoride. Resin represents photopolymer resin.
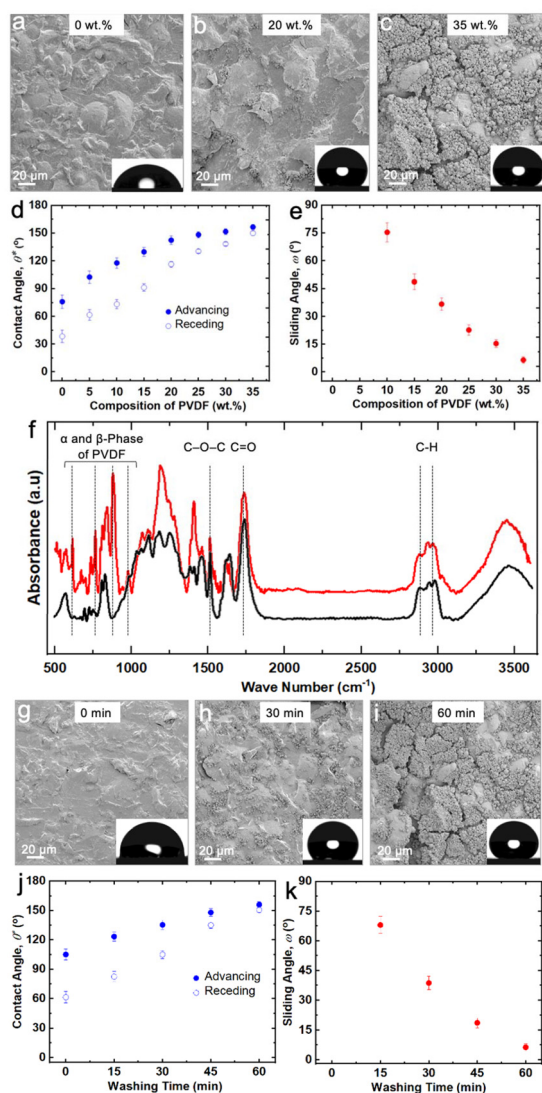
Fig. 2 Surface morphology and liquid repellency. SEM images of (a) photopolymer resin, (b) photopolymer resin + 20 wt% PVDF, and (c) photopolymer resin + 35 wt% PVDF. Inset shows contact angle images. (d) Advancing and receding contact angles, and (e) sliding angles of ~20 μL water droplets on 3D printed objects with different PVDF compositions. Error bars represent SD. (f) FTIR spectra of 3D printed objects with photopolymer resin (black) and photopolymer resin + 35 wt% PVDF (red). SEM images of photopolymer resin + 35 wt% PVDF with (g) 0 min, (h) 30 min, and (i) 60 min washing times. Inset shows contact angle images. (j) Advancing and receding contact angles, and (k) sliding angles of ~20 μl water droplets on 3D printed objects with different washing times. Error bars represent SD. Scale bars for a–c and g–i are 20 μm.

roughness increased due to more PVDF particles on the surface (Fig. 2b and c), the apparent contact angles increased (Fig. 2d), and the sliding angles decreased (Fig. 2e). For example, at an intermediate composition of 20 wt% PVDF, the surfaces were rougher (Fig. 2b; R_{rms} = 45 ± 3.1 μm), and more hydrophobic (θ^*_{adv} = 145°, θ^*_{rec} = 108°, ω = 34°) compared to 0 wt% PVDF. However, at this intermediate composition of 20 wt% PVDF, the texture was not optimal to impart

sufficiently low solid–liquid interfacial area in the Cassie-Baxter state to result in superhydrophobicity. At a high composition of 35 wt% PVDF, the surface roughness was higher (Fig. 2c; R_{rms} = 100 ± 3.6 μm), and the texture imparted sufficiently low solid–liquid interfacial area in the Cassie-Baxter state to result in superhydrophobicity with very high apparent contact angles and very low sliding angles (θ^*_{adv} = 156°, θ^*_{rec} = 150°, ω = 8°). Our sliding angle measurements matched reasonably well with the theoretical predictions based on a balance between work done by gravity and work expended due to adhesion (ESI section S1†). The superhydrophobicity of the photopolymer resin + 35 wt% PVDF is due to the appropriate combination of surface texture and low solid surface energy imparted by PVDF particles. The surface texture imparted by PVDF particles was also evident in the cross-sectional surface morphology (ESI section S2†). Furthermore, the presence of PVDF particles at the surface with increasing PVDF composition was also evident from Fourier transform infrared spectroscopy (FTIR). While the FTIR spectra (Fig. 2f) of just the photopolymer resin (i.e., 0 wt% PVDF) displayed only the stretching vibrations of C=O at 1156 cm⁻¹, C–O–C at 1728 cm⁻¹ and C–H bonds at 2900 cm⁻¹ of acrylic ester groups,[44] the FTIR spectra of the photopolymer resin + 35 wt% PVDF displayed absorption peaks at 796 cm⁻¹, 975 cm⁻¹, 1402 cm⁻¹ corresponding to α-phase of PVDF and at 878 cm⁻¹, 1072 cm⁻¹ and 1170 cm⁻¹ corresponding to β-phase of PVDF (Fig. 2f and ESI section S3†).[45] At compositions significantly higher than 35 wt% PVDF, 3D printing was intractable due to high viscosity of the ink. Based on these results, we chose 35 wt% PVDF for subsequent experiments to fabricate superhydrophobic 3D objects.

In addition to composition of the ink, washing time (with acetone) is another key parameter influencing the surface texture (and hence superhydrophobicity). To systematically investigate the influence of washing time on superhydrophobicity, we 3D printed simple cuboid-shaped objects with photopolymer resin + 35 wt% PVDF blends at different washing times. To assess the wetting properties of the 3D printed cuboids, we measured the contact angles and sliding angles with ~20 μL water droplets. Without any washing, (i.e., 0 min), the surfaces of the 3D printed cuboids displayed low roughness (Fig. 2g; R_{rms} = 28 ± 1.9 μm) and hydrophobicity with apparent contact angle θ^* = 102° (Fig. 2j). As the washing time increased, the surface roughness increased due to more PVDF particles on the surface (Fig. 2h and i), and the apparent contact angles increased (Fig. 2j). For example, at an intermediate washing time of 30 min, the surfaces were rougher (Fig. 2h; R_{rms} = 65 ± 2.7 μm), and more hydrophobic (θ^*_{adv} = 135°, θ^*_{rec} = 105°, ω = 35°) compared to surfaces without any washing. However, at this intermediate washing time of 30 min, the texture was not optimal to impart sufficiently low solid–liquid interfacial area in the Cassie-Baxter state to result in superhydrophobicity. At a high washing time of 60 min, the surface roughness was higher (Fig. 2i; R_{rms} = 100 ± 3.6 μm), and the texture imparted

sufficiently low solid–liquid interfacial area in the Cassie-Baxter state to result in superhydrophobicity with very high apparent contact angles and very low sliding angles (θ^*_{adv} = 156°, θ^*_{rec} = 150°, ω = 8°). At washing times significantly higher than 60 min, acetone (a good solvent for acrylic-based photopolymer resins) compromised the shape and structural integrity of the 3D printed objects. Based on these results, we chose 60 min washing time for fabricating superhydrophobic 3D objects.

Utilizing the inexpensive 3D printer and the optimal combination of ink composition and washing time, we printed a broad range of complex 3D shapes (Fig. 3a–f and ESI section S4†), including a moon, a five-triangle star, a heart, a chess rook, a boat, a multi-petal flower, a honeycomb matrix, an aircraft, a boat, a spoon and a truncated cone with superhydrophobic surfaces. Our 3D printed structures displayed superhy-

drophobicity, which is evident from water droplets (blue) beading up and bouncing on the surface (Fig. 3g). Note that the contact time of the droplets during bouncing is on the order of 10 ms, which agrees with prior literature.[46,47] In addition to water, we also investigated the repellency of our 3D printed structures to various water + sodium dodecyl sulfate (SDS) solutions. Apparent contact angle and sliding angle measurements with ~20 μL droplets of water + SDS solutions indicated that our 3D printed structures displayed super-repellency for liquids with $\gamma_{lv} \geq$ 55 mN m^{-1} (e.g., θ^*_{adv} = 153°, θ^*_{rec} = 145°, ω = 8° for water + 2 mM SDS with $\gamma_{lv} \approx$ 55 mN m^{-1}; Fig. 3i). This is also evident from water + 2 mM SDS droplets (red) bouncing on the surface (Fig. 3h). Furthermore, our 3D printed structures displayed super-repellency to aqueous liquids with a wide range of pH values (acidic, neutral, and basic), indicating their resistance to chemical damage by
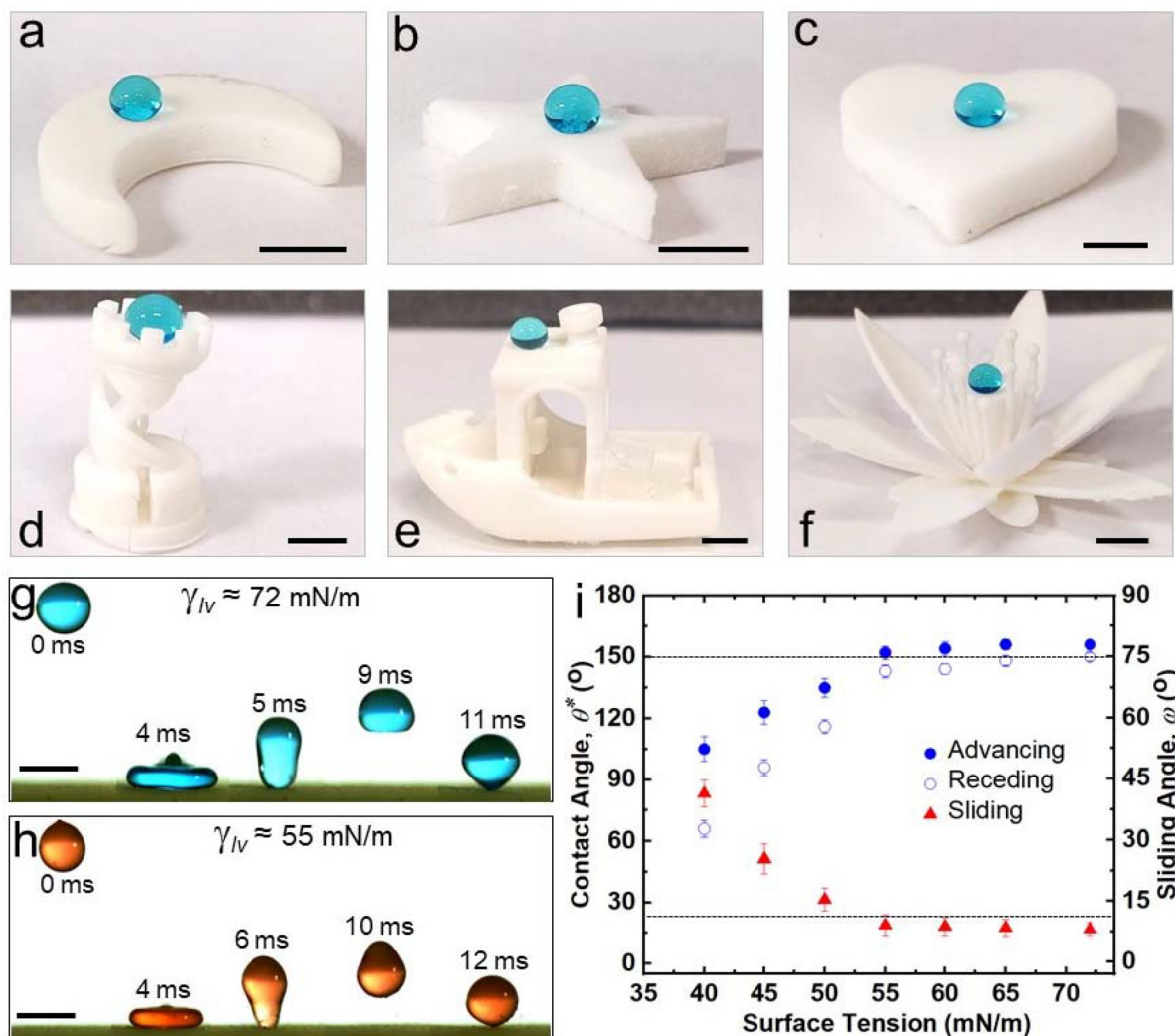

Fig. 3 3D printed superhydrophobic objects. (a–f) Droplets of water adopting the Cassie-Baxter state and beading up on various 3D printed superhydrophobic geometries. Series of images illustrating droplets of (g) water (blue), and (h) water + 2 mM SDS (red) bouncing on 3D printed superhydrophobic objects. (i) Advancing and receding contact angles as well as sliding angles of aqueous liquids with different surface tensions on 3D printed superhydrophobic objects. Error bars represent SD. Scale bars for a–f represent 5 mm. Scale bars for g and h represent 1 mm.

aqueous corrosive liquids (ESI section S5†) as well as resistance to simple blade scratch (ESI section S6†). To reiterate, our vat photopolymerization 3D printing technique to fabricate superhydrophobic structures is devoid of expensive instrumentation or multi-component inks or multi-step processing.

Super-repellency of our 3D printed structures to a wide variety of aqueous liquids enables easy droplet manipulation. To demonstrate this, we 3D printed serpentine and Y-shaped superhydrophobic grooves, placed them on an inclined plane and sequentially dispensed a droplet of $FeCl_3$ (yellow) and a droplet of NaOH (colorless) at the top of the groove (Fig. 4a and b). As anticipated, both the droplets rapidly rolled down the inclined groove (velocity ≈ 8 mm s^{-1} for ~ 20 μL droplets), due to gravity and merged at the bottom of the groove. Upon merging, the droplet turned brownish red color, owing to the reaction between Fe^{3+} and OH^{-}.[48] In this manner, our simple and inexpensive 3D printed superhydrophobic structures can be used to manipulate aqueous droplets for potential applications in lab-on-chip systems. While our 3D printed structures displayed super-repellency for liquids with $\gamma_{lv} \geq 55$ mN m^{-1}, oils and organic solvents (with $\gamma_{lv} < 30$ mN m^{-1}) adopted

the Wenzel state and completely wet our 3D printed structures ($\theta^{\star} = 0°$). Utilizing such selective wettability (*i.e.*, superhydrophobicity and superoleophilicity),[22,23,49] it is possible to selectively absorb oils and organic solvents from water (materials and methods). To accomplish this, we 3D printed porous cuboids (~ 10 mm × 10 mm × 10 mm) that are superhydrophobic and superoleophilic (Fig. 4c and d). Upon immersing them in a mixture of water (blue) and hexane (red; floating on water), the 3D printed porous cuboids completely absorbed the hexane, but did not absorb any water (Movie S1†). Similarly, upon immersing them in a mixture of water (blue) and chloroform (red; submerged in water), the 3D printed porous cuboids completely absorbed the chloroform, but did not absorb any water (Movie S2†). In this manner, our inexpensive 3D printing technique allows fabrication of structures for separation of oils and organic solvents from water.

To demonstrate the versatility of our inexpensive 3D printing technique, we also fabricated multifunctional complex 3D structures/shapes with superhydrophobicity as well as magnetic or color morphing properties. To accomplish this, we modified the inks used for printing superhydrophobic objects by adding Fe_3O_4 nanoparticles (for magnetic properties) or photochromic/thermochromic pigments (for color morphing properties). Since low surface energy is a requirement for superhydrophobicity, we fluorinated the Fe_3O_4 nanoparticles and the photochromic/thermochromic pigments with heptadecafluoro-1,1,2,2-tetrahydrodecyl trichlorosilane to impart low surface energy (materials and methods). Here, it must be noted that too high of a filler composition (PVDF or fluorinated Fe_3O_4 or fluorinated photochromic/thermochromic pigments) makes 3D printing intractable due to high viscosity of the ink, and too low of a filler composition in the ink leads to non-uniform or insufficient magnetic or photochromic or superhydrophobic properties. Based on this understanding, as an example, we fabricated magnetic superhydrophobic structures using photopolymer resin + 20 wt% PVDF + 5 wt% fluorinated Fe_3O_4 blends. All complex 3D structures/shapes (moon, five-triangle star, heart, chess rook, boat, and dumbbell) printed with this blend displayed superhydrophobicity ($\theta^{\star}_{adv} = 155°$, $\theta^{\star}_{rec} = 148°$, $\omega = 7°$; Fig. 5a–e). In addition, when a magnet was brought into the vicinity, all complex 3D structures/shapes immediately adhered to it, confirming the magnetic property and upon detaching from the magnet, the surfaces retained their superhydrophobicity. Here, it is important to note that there is virtually no difference in the mechanical properties (Young's modulus and % strain to failure) of our 3D printed superhydrophobic structures before and after addition of fluorinated Fe_3O_4 (ESI section S7†). In a similar manner, we fabricated photochromic complex 3D printed superhydrophobic structures using photopolymer resin + 20 wt% PVDF + 5 wt% fluorinated photochromic pigment blends. All complex 3D structures/shapes printed with this blend displayed superhydrophobicity ($\theta^{\star}_{adv} = 156°$, $\theta^{\star}_{rec} = 148°$, $\omega = 8°$; Fig. 5d). In addition, when exposed to 365 nm UV light, these complex 3D structures/shapes rapidly changed color from light brown to
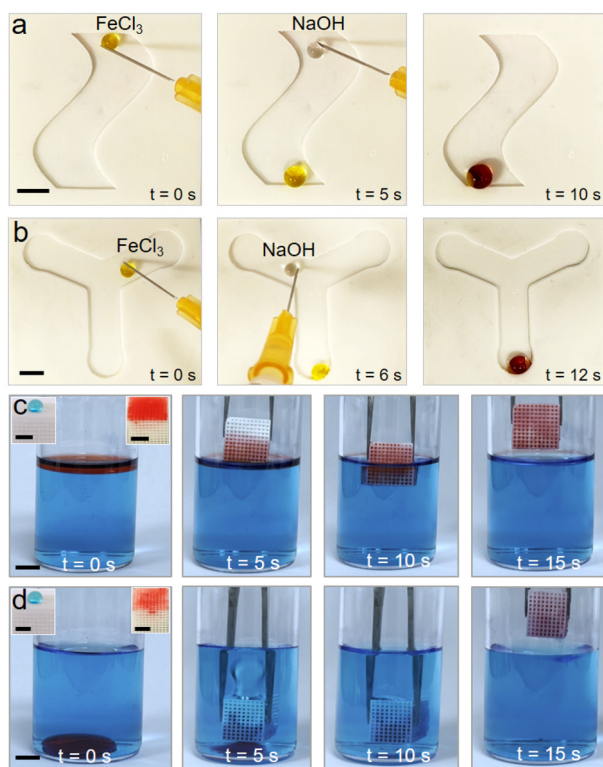

Fig. 4 Droplet manipulation and oil–water separation. (a) and (b) Series of images illustrating an $FeCl_3$ droplet (yellow) and an NaOH droplet (colorless) rolling down and merging in a 3D printed superhydrophobic groove with a serpentine shape and Y-shape, respectively. Series of images illustrating the (c) separation of hexane (red, floating on water) from water (blue), and (d) separation of chloroform (red, submerged in water) from water (blue). Insets show a water droplet (blue) beading up and hexane or chloroform droplet (red) completely spreading. Scale bars represent 5 mm.
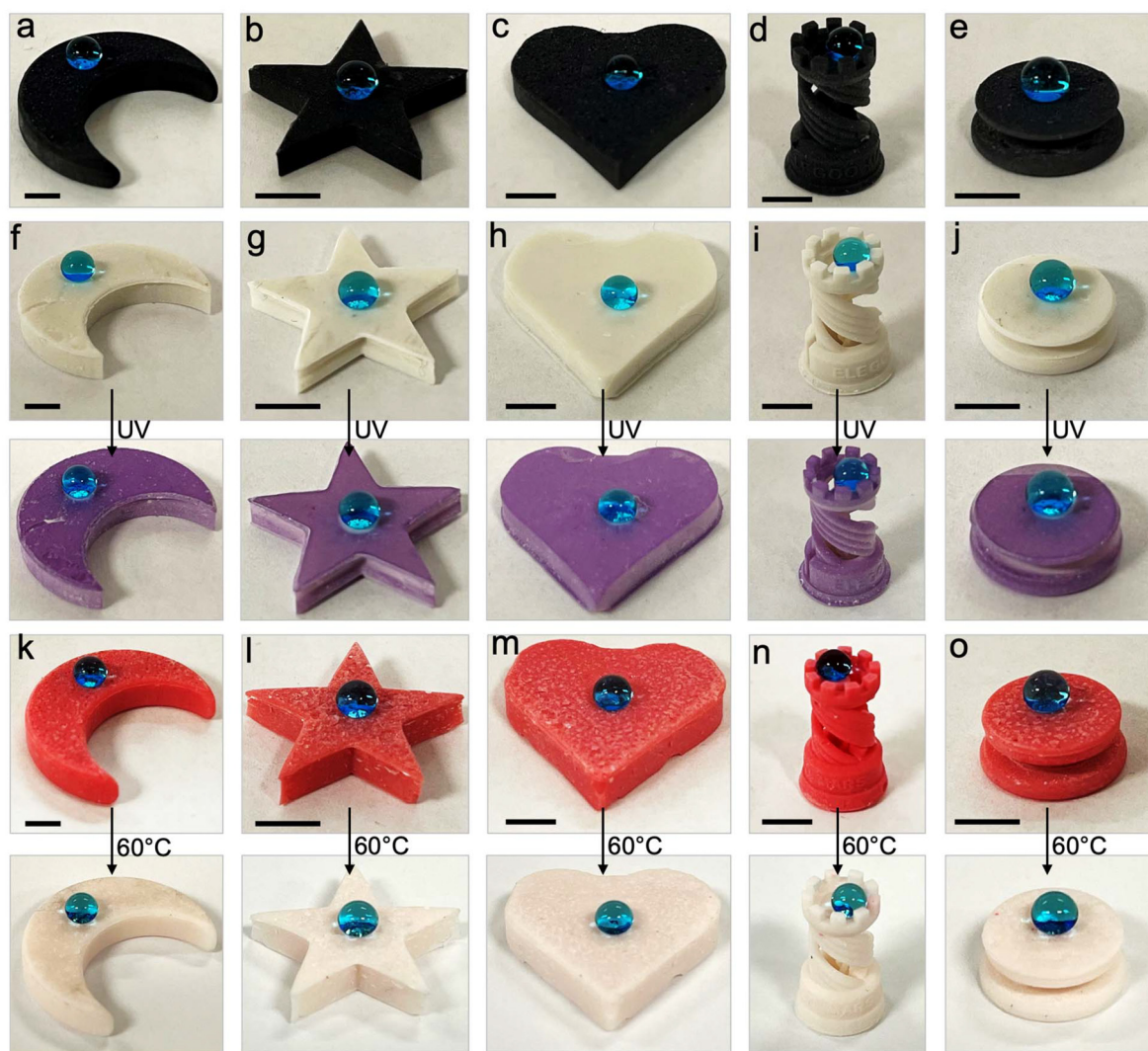
Fig. 5 3D printed multifunctional objects. Water droplets (blue) beading up on 3D printed objects of different geometries. (a–e) Magnetic superhydrophobic objects, (f–j) photochromic superhydrophobic objects, before UV exposure (white) and after UV exposure (violet), and (k–o) thermochromic superhydrophobic objects, at 25 °C (red) and at 80 °C (white). Scale bars represent 5 mm.

violet, while retaining their superhydrophobicity (Fig. 5f–j). Upon turning off the UV light, the 3D structures/shapes rapidly reverted from violet to light brown, and the surface retained its superhydrophobicity. Finally, we fabricated complex 3D printed thermochromic superhydrophobic structures using photopolymer resin + 20 wt% PVDF + 5 wt% fluorinated thermochromic pigment blends. All complex 3D structures/shapes printed with this blend displayed superhydrophobicity ($\theta^*_{adv} = 156°$, $\theta^*_{rec} = 148°$, $\omega = 7°$; Fig. 5k–o). In addition, when heated from room temperature to 80 °C, these complex 3D structures/shapes gradually changed color from red to light pink, while retaining their superhydrophobicity. Upon cooling down to room temperature, the 3D structures/shapes gradually reverted from light pink to red, and the surface retained its superhydrophobicity. In this manner, we fabricated multifunctional 3D structures with

superhydrophobicity as well as magnetic or color morphing properties.

3. Conclusions

In summary, we fabricated 3D printed superhydrophobic objects with complex shapes and geometries using a very low-cost 3D printer, with an ink that consists of only two commercially-available components, and a process that consists of only two steps. We demonstrated that the optimal combination of ink composition and washing time is essential to achieve superhydrophobic 3D printed objects. Utilizing our inexpensive and simple technique, we demonstrated the fabrication of 3D objects with complex shapes and geometries that are super-repellent to liquids of surface tension $\gamma_{lv} \geq 55$ mN

m^{-1}. Finally, by modifying the inks with magnetic particles or photochromic/thermochromic dyes, we also fabricated complex multifunctional 3D printed objects with superhydrophobicity as well as magnetic or color morphing properties. We envision that our simple and inexpensive 3D printing technique will democratize the fabrication of superhydrophobic and multi-functional objects by enabling access to a wide range of end-users, especially in cost-constrained or skill-constrained environments.

4. Experimental

4.1. Fabrication of 3D printed superhydrophobic objects

A commercially available vat photopolymerization 3D printer (Elegoo Mars 2 Pro) was used for the 3D printing experiments. The printer is based on an LCD projector with a wavelength of 405 nm. The ink used for 3D printing superhydrophobic objects was prepared by mixing polyvinylidene fluoride (PVDF; molecular weight, $M_w \sim 530\,000$ Da; Scientific Polymers) particles in a photopolymer resin (Elegoo white; hardness: 84D, viscosity: 150–200 mPa s, liquid density: 1.10 g cm^{-3}, solid density: 1.19 g cm^{-3}) by magnetic stirring for 30 min. For 3D printing magnetic superhydrophobic objects, the ink was prepared by mixing fluorinated iron oxide (Fe$_3$O$_4$; Fisher) nanoparticles (50 to 100 nm) and PVDF particles in the photopolymer resin by magnetic stirring for 30 min. For 3D printing photochromic/thermochromic superhydrophobic objects, the ink was prepared by mixing fluorinated photochromic pigment (S62017; Atlanta Chemicals)/thermochromic pigment (TP31; Atlanta Chemicals) and PVDF particles in the photopolymer resin by magnetic stirring for 30 min. The Fe$_3$O$_4$ nanoparticles and photochromic/thermochromic pigments were fluorinated by modifying their surface *via* liquid phase silanization with heptadecafluoro-1,1,2,2-tetrahydrodecyl trichlorosilane (Gelest) in hexane (Fisher) for 12 h. Then, the appropriate ink (~50 mL) was transferred to the resin tank of the 3D printer. The 3D objects with different geometries were designed using a computer-aided design software (SolidWorks). The resulting STL files were sliced into a series of 2D layers of 100 μm thickness using a slicing software (Chitubox). Then, the resulting CBDDLP files were transferred to the printer *via* USB. After 3D printing, the objects were carefully separated from the build platform, immersed in acetone (Fisher) for washing away the unreacted polymer resin, and subsequently dried at ambient conditions.

4.2. Contact angle and sliding angle measurements

Contact angles and sliding angles of different liquids were measured using a goniometer (Ramé-Hart 260-F4). Contact angles were measured by advancing or receding a small volume of liquid (~20 μL) onto the surface using a micrometer syringe (Gilmont). Sliding angles were measured by slowly tilting the stage until the droplet (~20 μL) rolled off from the surface. All results are the average of three individual measurements.

4.3. Morphology characterization

Surface morphology was characterized using a scanning electron microscope (SEM; Thermofisher Phenom Pharos) at 2 kV with a secondary electron detector. The samples were sputter coated with a thin film of gold prior to imaging (Cressington 108).

4.4. Surface roughness measurement

All surface roughness measurements were conducted with a 3D optical surface profiler (Filmetrics Profilm3D). In each measurement, 3D printed polymeric samples (10 mm × 10 mm) were placed on a motorized stage, focused and scanned at 50× magnification with Nikon Mirau interferometry objective lens. Each surface profile was averaged over 8 frames and acquired using a peak valley envelope setting. Images were processed and root mean square roughness was determined with Profilm Software (Filmetrics, San Diego, CA, USA). All results are the average of three individual measurements.

4.5. FTIR characterization

Samples for FTIR (Thermo Scientific Nicolet iS50) were prepared by mixing the desired material with KBr powder to form a pellet. Samples were analyzed with DTGS/KBr detector, and spectra were recorded at 2 cm^{-1} resolution with 32 scans. Background spectra were obtained with an empty pellet holder.

4.6. Droplet bouncing

Movies of bouncing droplets were obtained using a high-speed camera (Fastcam Mini AX200) at 1000 frames per second.

4.7. Oil–water separation

To demonstrate oil–water separation, water (dyed blue with methylene blue) and 1 mL of hexane or chloroform (dyed red with Oil Red O) were placed in glass vial. Then, 3D printed superhydrophobic porous cuboid was immersed in the oil–water mixture to selectively absorb oil.

4.8. Magnetic actuation and color morphing

Magnetic actuation was performed by exposing 3D printed magnetic superhydrophobic objects to neodymium block magnet (Applied Magnets). Color morphing was performed by irradiating 3D printed photochromic superhydrophobic objects with a 365 nm UV torch (Tattu) and heating 3D printed thermochromic superhydrophobic objects on a hot plate (Fisher).

4.9. Tensile testing

We measured the quasi-static mechanical properties of the 3D printed structures using ASTM Type I specimens in a tensile tester (F505, Mark-10).[50,51] Force was measured with a load cell (1 kN, FS05-200, Mark-10) and displacement was measured using the crosshead velocity (2 mm min^{-1}). Specimen dimensions were measured with calipers (Fisher) and used to convert the force-displacement curves to stress–strain curves.

Author contributions

A. K. K. conceived the idea. A. M. R., M. B., M. Z., Y. J. K. and S. V. conducted the experiments. A. M. R., M. B., M. Z., Y. J. K., S. V. and A. K. K. conducted the analysis. A. M. R., M. B., M. Z., Y. J. K., S. V. and A. K. K. wrote the manuscript. All authors contributed to the manuscript and have approved the final version of the manuscript.

Data availability

The authors confirm that all the data supporting this work is included within the article and the ESI.† Additional data are available from the corresponding author A. K. K., upon reasonable request.

Conflicts of interest

The authors declare no conflict of interest.

Acknowledgements

References

1 S. C. Ligon, R. Liska, J. r. Stampfl, M. Gurr and R. Mülhaupt, *Chem. Rev.*, 2017, **117**, 10212–10290.
2 J. R. Tumbleston, D. Shirvanyants, N. Ermoshkin, R. Janusziewicz, A. R. Johnson, D. Kelly, K. Chen, R. Pinschmidt, J. P. Rolland and A. Ermoshkin, *Science*, 2015, **347**, 1349–1352.
3 D. A. Walker, J. L. Hedrick and C. A. Mirkin, *Science*, 2019, **366**, 360–364.
4 M. Regehly, Y. Garmshausen, M. Reuter, N. F. König, E. Israel, D. P. Kelly, C.-Y. Chou, K. Koch, B. Asfari and S. Hecht, *Nature*, 2020, **588**, 620–624.
5 S. Deng, J. Wu, M. D. Dickey, Q. Zhao and T. Xie, *Adv. Mater.*, 2019, **31**, 1903970.
6 G. Zhu, Y. Hou, J. Xu and N. Zhao, *Adv. Funct. Mater.*, 2021, **31**, 2007173.
7 H. Quan, T. Zhang, H. Xu, S. Luo, J. Nie and X. Zhu, *Bioact. Mater.*, 2020, **5**, 110–115.
8 E. Fantino, A. Chiappone, I. Roppolo, D. Manfredi, R. Bongiovanni, C. F. Pirri and F. Calignano, *Adv. Mater.*, 2016, **28**, 3712–3717.
9 N. A. Traugutt, D. Mistry, C. Luo, K. Yu, Q. Ge and C. M. Yakacki, *Adv. Mater.*, 2020, **32**, 2000797.
10 X. Mu, T. Bertron, C. Dunn, H. Qiao, J. Wu, Z. Zhao, C. Saldana and H. Qi, *Mater. Horiz.*, 2017, **4**, 442–449.
11 Y. Zhang, M.-J. Yin, X. Ouyang, A. P. Zhang and H.-Y. Tam, *Appl. Mater. Today*, 2020, **19**, 100580.
12 Z. Dong, M. Vuckovac, W. Cui, Q. Zhou, R. H. Ras and P. A. Levkin, *Adv. Mater.*, 2021, **33**, 2106068.
13 G. Kaur, A. Marmur and S. Magdassi, *Addit. Manuf.*, 2020, **36**, 101669.
14 W. Deng, Y. Liu, Y. Rui, G. Lu and J. Liu, *Prog. Org. Coat.*, 2023, **181**, 107570.
15 D. Zang, R. Zhu, W. Zhang, X. Yu, L. Lin, X. Guo, M. Liu and L. Jiang, *Adv. Funct. Mater.*, 2017, **27**, 1605446.
16 A. M. Rather and U. Manna, *J. Mater. Chem. A*, 2017, **5**, 15208–15216.
17 A. M. Rather, N. Jana, P. Hazarika and U. Manna, *J. Mater. Chem. A*, 2017, **5**, 23339–23348.
18 X. Yao, Y. Song and L. Jiang, *Adv. Mater.*, 2011, **23**, 719–734.
19 W. Feng, E. Ueda and P. A. Levkin, *Adv. Mater.*, 2018, **30**, 1706111.
20 A. Neto, P. Levkin and J. Mano, *Mater. Horiz.*, 2018, **5**, 379–393.
21 R. B. Channon, R. F. Menger, W. Wang, D. B. Carrão, S. Vallabhuneni, A. K. Kota and C. S. Henry, *Microfluid. Nanofluid.*, 2021, **25**, 1–8.
22 L. Feng, Z. Zhang, Z. Mai, Y. Ma, B. Liu, L. Jiang and D. Zhu, *Angew. Chem.*, 2004, **116**, 2046–2048.
23 S. Movafaghi, M. D. Cackovic, W. Wang, H. Vahabi, A. Pendurthi, C. S. Henry and A. K. Kota, *Adv. Mater. Interfaces*, 2019, **6**, 1900232.
24 Y. Zhu, J. Zhang, Y. Zheng, Z. Huang, L. Feng and L. Jiang, *Adv. Funct. Mater.*, 2006, **16**, 568–574.
25 D. Yan, J. Lin, B. Zhang, S. Zhang, S. Ling and J. Song, *J. Mater. Chem. A*, 2024, **12**, 19268–19276.
26 D. Yan, Y. Lu, J. Lin, W. Li and J. Song, *Appl. Phys. Lett.*, 2024, **125**, 071601.
27 Y. Thomas, *Philos. Trans. R. Soc. London*, 1805, **95**, 65–87.
28 A. K. Kota, G. Kwon and A. Tuteja, *NPG Asia Mater.*, 2014, **6**, e109–e109.
29 T. Huhtamäki, X. Tian, J. T. Korhonen and R. H. Ras, *Nat. Protoc.*, 2018, **13**, 1521–1538.
30 W. Wang, H. Vahabi, S. Movafaghi and A. K. Kota, *Adv. Mater. Interfaces*, 2019, **6**, 1900538.
31 J. Genzer and K. Efimenko, *Science*, 2000, **290**, 2130–2133.
32 A. Marmur, *Langmuir*, 2003, **19**, 8343–8348.
33 H. Vahabi, W. Wang, K. C. Popat, G. Kwon, T. B. Holland and A. K. Kota, *Appl. Phys. Lett.*, 2017, **110**, 251602.
34 R. N. Wenzel, *Ind. Eng. Chem.*, 1936, **28**, 988–994.
35 A. Cassie and S. Baxter, *Trans. Faraday Soc.*, 1944, **40**, 546–551.
36 S. Vallabhuneni, S. Movafaghi, W. Wang and A. K. Kota, *Macromol. Mater. Eng.*, 2018, **303**, 1800313.

37 K. Golovin, D. H. Lee, J. M. Mabry and A. Tuteja, *Angew. Chem.*, 2013, **125**, 13245–13249.

38 W. Wang, J. Salazar, H. Vahabi, A. Joshi-Imre, W. E. Voit and A. K. Kota, *Adv. Mater.*, 2017, **29**, 1700295.

39 B.-X. Zhang, S.-L. Wang and X.-D. Wang, *Langmuir*, 2019, **35**, 662–670.

40 H. Y. Erbil and C. E. Cansoy, *Langmuir*, 2009, **25**, 14135–14145.

41 R. J. Vrancken, H. Kusumaatmaja, K. Hermans, A. M. Prenen, O. Pierre-Louis, C. W. Bastiaansen and D. J. Broer, *Langmuir*, 2010, **26**, 3335–3341.

42 J. Zhang, Y. Chen, Y. Zhang, S. Wu, J. Sun, X. Liu and J. Song, *Adv. Funct. Mater.*, 2024, 2400024.

43 M. Wang, J. Hu, Y. Wang and Y.-T. Cheng, *J. Electrochem. Soc.*, 2019, **166**, A2151.

44 G. Arias-Ferreiro, A. Ares-Pernas, A. Lasagabáster-Latorre, N. Aranburu, G. Guerrica-Echevarria, M. S. Dopico-García and M.-J. Abad, *Polymers*, 2021, **13**, 2068.

45 I. Y. Abdullah, M. Yahaya, M. H. H. Jumali and H. M. Shanshool, *AIP Conf. Proc.*, 2014, **1614**, 147.

46 J. C. Bird, R. Dhiman, H.-M. Kwon and K. K. Varanasi, *Nature*, 2013, **503**, 385–388.

47 D. Richard, C. Clanet and D. Quéré, *Nature*, 2002, **417**, 811–811.

48 Y. Yang, X. Li, X. Zheng, Z. Chen, Q. Zhou and Y. Chen, *Adv. Mater.*, 2018, **30**, 1704912.

49 S. Wu, D. Yan, Y. Chen and J. Song, *Nano Energy*, 2024, **119**, 109066.

50 A. L. Gershon, D. P. Cole, A. K. Kota and H. A. Bruck, *J. Mater. Sci.*, 2010, **45**, 6353.

51 A. L. Gershon, A. K. Kota and H. A. Bruck, *J. Compos. Mater*, 2009, **43**, 2587.